CCFE
CULHAM CENTRE FOR FUSION ENERGY

UK Atomic Energy Authority

UKAEA-CCFE-PR(21)25

J. Lion, F. Warmer, H. Wang, C.D. Beidler, S.I. Muldrew, R. C. Wolf

A general stellarator version of the systems code PROCESS

Enquiries about copyright and reproduction should in the first instance be addressed to the UKAEA Publications Officer, Culham Science Centre, Building K1/0/83 Abingdon, Oxfordshire, OX14 3DB, UK. The United Kingdom Atomic Energy Authority is the copyright holder.

The contents of this document and all other UKAEA Preprints, Reports and Conference Papers are available to view online free at scientific-publications.ukaea.uk/

A general stellarator version of the systems code PROCESS

J. Lion, F. Warmer, H. Wang, C.D. Beidler, S.I. Muldrew, R. C. Wolf

This is a preprint of a paper submitted for publication in Nuclear Fusion

A general stellarator version of the systems code PROCESS

J. Lion[a], F. Warmer[a], H. Wang[1], C.D. Beidler[a], S.I. Muldrew[b], R. C. Wolf[a]

[a] *Max Planck Institute for Plasmaphysics, Greifswald, Germany*
[b] *Culham Centre for Fusion Energy, UK Atomic Energy Authority, Culham Science Centre, Abingdon, Oxfordshire, OX14 3DB, UK*
[c] *Dept. of Physics, Yale University, New Haven, CT 06520, USA*

Abstract

We present modifications of the systems code PROCESS that allow for a description of a general class of stellarator power plants, based on a stellarator coil-set and the respective MHD plasma equilibrium. For this, we modify PROCESS such that each stellarator configuration enters the systems code via a set of effective parameters which can be calculated in advance before using them in new scaling models in PROCESS. Further, we show two applications of the new PROCESS version: We apply the code to, firstly, three reactor-size stellarator devices with different aspect ratios, and secondly, to three coil-sets optimized for the same equilibrium with varying coil numbers as obtained by stellarator optimization.

1. Introduction

Stellarators are attractive candidates for a fusion power plant: They operate in steady-state and can be optimized for minimal plasma current thus avoiding current driven instabilities. They do not rely on large poloidal field coils or a central solenoid. Stellarators also benefit from large connection lengths in island divertor configurations easing power exhaust. The lack of an inherent density limit allows higher fusion power at moderate temperatures. Finally, the highly dimensional design space can be utilised to optimise the configuration according to relevant physics and engineering requirements at the cost of geometrical complexity.

The recent start of operation of the prototype advanced stellarator Wendelstein 7-X (W7-X) has shown that such configurations can be realized with

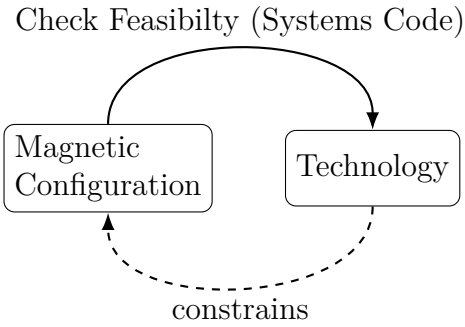

Figure 1: A systems code provides insights in feasibility of a magnetic stellarator configuration with respect to technology and can be used to constrain a magnetic configuration.

sufficient engineering accuracy [1, 2] providing further incentive to study fusion power plant designs based on stellarators.

As of now, attractive stellarator configurations are developed through the process of *stellarator optimization* [3, 4, 5, 6, 7], where a computational framework optimises a three-dimensional MHD equilibrium and a corresponding coil set to fulfill a set of mostly physics-related figures of merit. These configurations have a fixed size, aspect ratio, and operation point. To our knowledge, there exists so far no systematic framework that checks a configuration perceived through stellarator optimisation for a broader range of engineering constraints specific to fusion reactor design such as superconductor or neutronic limitations. As the resulting configurations are a fixed design point, there is currently no framework available capable of quickly exploring a larger design space, while simultaneously judging the technological and economical feasibility of regions of the design space. Systems codes can fill this gap.

Systems codes are coherent, holistic computational frameworks that aspire to model the crucial features of an engineered system. They typically consist of a set of simplified models that depict the governing design parameters and constraints. In the context of fusion power plants, the use of systems codes has several advantages:

1. They can check the feasibility of a given configuration in a holistic way
2. They can be used to find more technologically or economically suited design and operation points
3. They can easily adapt technological advances due to their modular structure

For tokamak fusion power plants, existing systems codes are e.g. PROCESS [8], SYCOMORE [9], MIRA [10] or BLUEPRINT [11]. Among these codes, PROCESS is predominantly used for the European studies of a tokamak demonstration power plant (DEMO) [12, 13, 14]. The wide use of PROCESS and the prospect of comparing stellarator and tokamak reactors in a comparable framework, makes PROCESS a well suited platform for the development of stellarator-specific systems code models. In fact, such attempts have already been made in a previous work [15, 16, 17], where PROCESS was modified to model five-periodic helical-axis advanced stellarators (HELIAS) based upon specific engineering studies of HELIAS-5B [18], a linear extrapolation along the Wendelstein line. In these earlier works it was found that PROCESS required stellarator-specific developments in mainly four models to reasonably reflect the features of a stellarator power plant, namely in the plasma geometry model, the modular coil model, the island divertor, and the plasma transport model.

The aim of this paper is to extend the functionality of the stellarator-specific systems code models to describe any *general* modular stellarator – using only a stellarator reference MHD equilibrium and the associated coil filaments as input.

The outline of this paper is as follows: In section 2 we describe the structural changes in PROCESS that were necessary to include more general stellarators. In section 3 we describe the newly developed models and their implementation. Finally, in section 4 we employ the PROCESS framework with the implemented stellarator-specific changes for three example studies: First, the new magnet system model is benchmarked against a tokamak reference case. Secondly, we model three different stellarator configurations with distinct aspect ratios, using a 3, 4 and 5 periodic HELIAS configuration. Thirdly, we vary the number of coils for a specific W7-X equilibrium and study the impact on the coil material properties.

2. New Workflow for stellarator - PROCESS

Stellarators, by their 3D geometry, impose non-trivial physics and engineering constraints on a fusion power plant design. For example, in contrast to tokamaks, the magnetic field strength on the inboard side of the coils is different for every coil, the divertor area depends on the location of the magnetic islands, or the neutron wall load has large variations not only in poloidal, but also in toroidal direction. Further, stellarators can have vastly

different coil and plasma boundary shapes. It is thus clear, that the accurate representation of systems codes relevant features at low computational cost is quite challenging for general stellarators. To mitigate this issue, we introduce an additional, automatized, calculation step between the output stemming from stellarator optimisation and the inputs that go into the systems code, as schematically shown in Figure 2. In practice, the work-flow then is as follows. 'Stellarator optimisation' provides a 3D MHD equilibrium and a set of corresponding, as fixed considered, coil filaments at a reference point in major radius and aspect ratio, from here on represented with the symbol $\mathfrak{C}$, which serves as input for the detailed calculations. The newly introduced intermediate calculation step (essentially the first part of the systems code models), involves accurate, but comparatively slow computations at this reference point. The result of these computations are a set of configuration dependent effective parameters $a_i(\mathfrak{C})$, which serve as input for exact, fitted, or empirical scaling equations in the systems code.

The general idea behind this approach is to separate computationally heavy operations from the systems code. This means that every stellarator-specific systems code model consists of essentially two parts. The first part entails the detailed modelling of a sub-system *outside* the systems code. The second part, in turn, involves an associated (fast) scaling equation *within* the systems code that makes use of the results from the detailed calculations. An example here would be the computation of the maximal coil force density $f_{max}(\mathfrak{C})$ as effective parameter from 3D calculations for a reference coil set. In this example the scaling of f_{max} within the systems code then is a linear scaling law in B_{max} and the current density j, both parameters that the systems code optimizes for.

We implement the systems code models in a way that they reflect extrapolations of the reference point $\mathfrak{C}$ in the following macroscopic design parameters: The major overall size of the machine (coil and plasma size), the minor plasma radius a at constant coil radius, and the total magnetic field strength on axis B_t. For the plasma design, the implemented scaling parameters are the plasma density, temperature, and the ISS04 'renormalization' factor (a measure for the configuration dependent quality of energy confinement [19]). The stellarator-PROCESS version is capable of optimizing for devices by scaling these parameters as a part of the optimization vector now.

In addition to the above listed set of iteration parameters, PROCESS also optimizes in the engineering parameter design space, with parameters such as

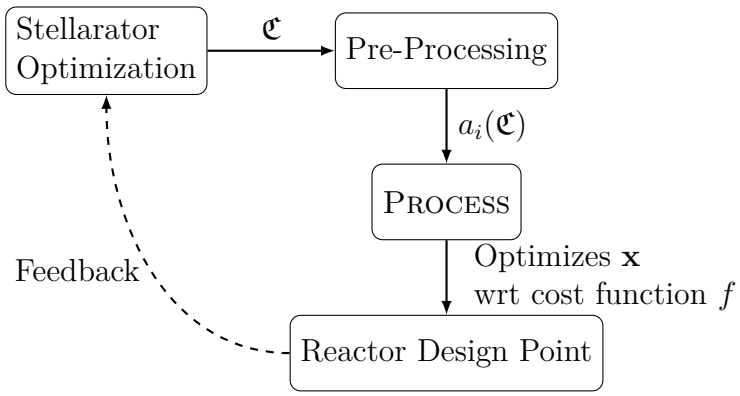

Figure 2: The workflow of the pre-calculation step: A configuration $\mathfrak{C}$ (coil filaments and flux surfaces) is assumed as input from stellarator optimization. A set of PROCESS relevant parameters a_i is calculated based on a reference point of $\mathfrak{C}$ which PROCESS uses to calculate and optimize an iteration vector $\mathbf{x}$ to reactor design point according to an objective function f and according to the applied constraints. The design point can be used again as feedback for stellarator optimization.

winding pack size, coil quench times, critical current density safety margins in the superconductor, copper fractions in the winding pack, net electricity output, etc., also see [8, 20].

Note that by this prescription the coil number and the coil shapes are considered fixed by stellarator-PROCESS and only the overall size of the coils is scaled. A broader device scan in different stellarator configurations or different coil-sets can be done by sampling different configurations $\mathfrak{C}$ using stellarator optimization.

3. Models

Below, we introduce the newly developed stellarator-specific systems code models that aim to describe a general class of stellarators with a modular coil set, irrespective of their shape. The stellarator modifications to PROCESS are comprehensive in the sense that they allow an equivalent modeling stellarators compared to the tokamak treatment [8, 20].

For each model we describe both the external procedure of calculating the effective parameters as well as the systems code internal scaling equations. The effective parameters that are calculated in the external step are distinguished into two categories. The first type are configuration-specific quantities, that are used directly in follow up calculations and these are de-

noted by $a_i(\mathfrak{C})$. The second type of parameters are those that are calculated as a reference point for the scaling equations and these are denoted as hatted values, $\hat{a_i}(\mathfrak{C})$, where $\mathfrak{C}$ represents the configuration stemming from stellarator optimisation (3D MHD equilibrium and associated coil filaments).

3.1. Plasma Volume and Surface

The plasma volume V and the plasma surface area S are basic properties in PROCESS. For example, subsequent calculations of the fusion power, fuelling rates, or material loads depend on the plasma volume. Similarly, the surface area is an important quantity to approximate the first wall area and to scale the heat flux densities.

The spatial location of stellarator-symmetric flux surfaces can be parametrized by a set of Fourier coefficients $R^c_{m,n}$ and $Z^s_{m,n}$, where m and n the poloidal and toroidal mode numbers respectively. The cylindrical coordinates for each flux surface can then be simply obtained by

$$R(s,u,v) = \sum_{m=0}^{m_{max}} \sum_{n=-n_{max}}^{n_{max}} R^c_{m,n}(s)\cos(mu - N_f n v), \tag{1}$$

$$Z(s,u,v) = \sum_{m=0}^{m_{max}} \sum_{n=-n_{max}}^{n_{max}} Z^s_{m,n}(s)\sin(mu - N_f n v). \tag{2}$$

Here, u describes a poloidal coordinate, v the polar toroidal coordinate, and s is a flux surface coordinate. Equation 1 and 2 hold for stellarator symmetric configurations with a field period symmetry of N_f.

Using this formulation, the volume enclosed by the last closed flux surface can be calculated for a reference case ($\hat{R}$, $\hat{a}$) according to

$$\begin{aligned}\hat{V}(\mathfrak{C}) &= \int \sqrt{g} ds du dv \\ &= \frac{1}{3}\int_0^{2\pi}\int_0^{2\pi} R\left(z\partial_u R - R\partial_u z\right) du dv.\end{aligned} \tag{3}$$

The surface area of a flux surface can be calculated by

$$\begin{aligned}\hat{S}(\mathfrak{C}) &= \int |\nabla s|\sqrt{g} du dv \\ &= \int_0^{2\pi}\int_0^{2\pi} \Big[R^2(\partial_u z)^2 + R^2(\partial_u R)^2 \\ &\quad + \left(\partial_v R\partial_z u - \partial_v z\partial_u R\right)^2\Big]^{\frac{1}{2}} du dv.\end{aligned} \tag{4}$$

The values $\hat{V}(\mathfrak{C})$ and $\hat{S}(\mathfrak{C})$ are calculated in the pre-processing step for a reference point in major radius $\hat{R}$ and minor radius $\hat{a}$. Within PROCESS, the plasma volume and surface area is then simply obtained by the following scaling equations,

$$V = \hat{V}(\mathfrak{C})\frac{R}{\hat{R}}\frac{a^2}{\hat{a}^2},\ S = \hat{S}(\mathfrak{C})\frac{R}{\hat{R}}\frac{a}{\hat{a}}. \tag{5}$$

3.2. 0D-Transport

The 0D-transport model in PROCESS imposes a power balance as an equality constraint,

$$P_{Loss} \stackrel{!}{=} P_{heat}. \tag{6}$$

The left hand side includes contributions from confinement loss, from bremsstrahlung P_{br}, line radiation P_{line} and synchrotron radiation P_{sync}. The right hand side includes heating from fusion alphas P_α, a term of charged non-alpha particle heating $P_{\neg\alpha}$ (e.g. in D-D fusion) and a term for auxiliary heating P_{aux}. Writing these expressions explicitly, Equation 6 becomes

$$P_{Loss}^{conf} + P_{br} + P_{line} + P_{sync} \stackrel{!}{=} f_\alpha P_\alpha + f_{\neg\alpha} P_{\neg\alpha} + P_{aux}. \tag{7}$$

Here, f_α is the fraction of the alpha particle energy that is deposited in the plasma, which is an input parameter in PROCESS and depends on the configuration. Similarly $f_{\neg\alpha}$ accounts for the particle confinement fraction of non-alpha particles. PROCESS' model for radiation losses (P_{br}, P_{line},P_{sync}) is described in [21, 22]. For P_{Loss}^{conf}, PROCESS uses the effective energy confinement time τ_E to determine the effective power transfer

$$P_{Loss}^{conf} \simeq P_{Loss}^{scaling} \equiv \frac{W}{\tau_E}, \tag{8}$$

where W is the total plasma energy. The energy confinement time τ_E is obtained via empirical scaling laws. The appropriate scaling law for stellarators is the so-called ISS04 scaling [19],

$$\tau_E^{ISS04} = 0.134\, f_{ren} a^{2.25} R_0^{0.64} \overline{n}_e^{0.52} B_t^{0.84} \iota_{2/3}^{0.41} P^{-0.64}, \tag{9}$$

where a is the minor radius, R_0 is the major radius, $\overline{n}$ is the line averaged electron density, B_t the toroidal magnetic field, $\iota_{2/3}$ is the rotational transform (at $s = 2/3$), P is the combined effective plasma heating, and f_{ren} is

a proportionality factor that measures the deviation from the ISS04 scaling law.

The stored energy W in Equation 8 is obtained from the imposed profiles for particle species averaged density n and temperature T:

$$W = V\frac{3}{2}\int_0^1 d\rho\sqrt{g(\rho)}n(\rho)T(\rho) \tag{10}$$

In stellarators, ρ is usually chosen as the effective radius, which fulfils

$$\sqrt{g(\rho)} \sim \rho. \tag{11}$$

The temperature and density profile shapes for the electrons are *input parameters* in PROCESS and can be specified using the parametric form

$$T_e(\rho) = T_0(1-\rho^2)^{\alpha_T} \tag{12}$$

$$n_e(\rho) = n_0(1-\rho^2)^{\alpha_n}. \tag{13}$$

PROCESS implements the ion profiles as (user defined) multiples of the electron profiles. These profiles are taken to compute the radiation terms in the left hand side of Equation 7, see [21].

It should be noted that the imposed profile shapes are not *per se* consistent with the implied heating schemes or transport properties. However, in practice, the profile shapes can be determined by transport simulations independent of the systems code. Results from such simulations can then be used as input for PROCESS, e.g. in profile shapes or heating source.

Equation 7 serves as equality constraint in PROCESS.

3.3. 0.5D Neoclassical transport model for stellarators

As PROCESS lets the user choose T_0, n_0, α_n and α_T in Equation 13 freely, we introduce a "sanity check" of the confinement time here against a neoclassical model. The energy balance equation in steady state is

$$-\nabla \cdot \mathbf{q} = p. \tag{14}$$

Here, $\mathbf{q}$ is the flux surface averaged energy flux and p stands for the flux surface energy density sources and sinks. If one assumes constant energy flux on a flux surface, integrating Equation 14 over a volume up to a radius ρ_x yields

$$q(r=\rho_x) = \frac{f_\alpha P_\alpha(\rho_x) - P_{rad}(\rho_x)}{S(\rho_x)}, \tag{15}$$

where $S(\rho_x)$ is the surface area at a radius ρ_x. P_{rad} is the radiation power and P_α is the alpha particle heating power, both integrated values in the of $S(\rho_x)$ enclosed volume. In PROCESS, we choose $\rho_x = \rho_{core}$, where ρ_{core} is an input parameter in PROCESS, which determines the radius of a binary 'core' treatment [8]. ρ_{core} is usually chosen in the order of ~ 0.6 ($\rho = 1$ matches with the last closed flux surface). The new model in PROCESS now calculates a maximal allowable q^{max} with the calculated heating and radiation power as

$$q^{max} = \left(f_\alpha \langle p_\alpha \rangle_V - \langle p_{rad} \rangle_V \right) \frac{V(\rho_{core})}{S(\rho_{core})}. \tag{16}$$

Here, $\langle p_{\alpha,rad} \rangle_V$ denotes the power density averaged over $V(\rho_{core})$.

The volume over surface ratio at ρ_{core} can be obtained (approximately) by scaling of Equation 5.

Equation 16 can be compared against heat fluxes q_{neo} from neoclassical theory, e.g. [23, 24]. In PROCESS we compare Equation 16 against a neoclassical *electron* flux [24]

$$q_{e,neo} = \sum_{i=1,2} n_e T_e D_{i,e} \left[\left(\frac{\partial_r n_e}{n_e} + \left(\frac{D_{i+1,e}}{D_{i,e}} - \frac{3}{2} \right) \frac{\partial_r T_e}{T_e} \right) \right], \tag{17}$$

with

$$D_{i,e} \equiv D_{i,e}(n,T) = \frac{2}{\sqrt{\pi}} \int_0^\infty D_{1/\nu} K^{i-\frac{1}{2}} e^{-K} dK, \tag{18}$$

$$D_{1/\nu} = \frac{4}{9\pi} (2\epsilon_{eff})^{\frac{3}{2}} \frac{K^2 T^2}{e^2 R_0^2 B_0^2} \frac{1}{\nu(n,T)}, \tag{19}$$

where we take the profile shapes as given by PROCESS and further assume the electrons to be in the $1/\nu$ regime and neglect the effect of the radial electrical field. $\epsilon_{eff} \equiv \epsilon_{eff}(\mathfrak{C})$ is the averaged effective helical ripple and is an input parameter, which is calculated for every configuration $\mathfrak{C}$.

$q_{e,neo}$ serves as an order of magnitude check for q^{max}, as a design point with $2\, q_{e,neo} \sim q^{max}$ indicates that profile gradients at the found design point cause similar purely neoclassical transport fluxes to q^{max} and would not allow for an (unknown) turbulent heat flux q^{turb}.

This way we try to circumvent the consistency issues and restrict profile gradients in the 0D transport model of PROCESS for stellarators.

3.4. Density Limit

The density in stellarators devices is, at least empirically, bound by the Sudo limit [25], which accounts for excessive impurity radiation at high edge densities. This limit is proposed in the parametric form as

$$n_c^{sudo}\left[10^{20}\mathrm{m}^{-3}\right] = 0.25\, P^{0.5}\, B^{0.5}\, a^{-1}\, R^{-0.5}. \tag{20}$$

Stellarator-Process can enforce this limit or multiples thereof. Note however, that Equation 20 was seen exceeded in W7-X and LHD [26, 27] and is likely dependent on edge impurity concentrations which are not governed by Equation 20.

There is however another density constraint, which is imposed by operational boundaries in ECRH heated stellarator devices [28]: For reactor scenarios, ECRH using the O1 mode appears to be most suitable as it heats the lowest resonance of the electron gyro-frequency and thus requires lower gyrotron frequencies than higher resonant heating schemes. O1 heating implies the operational constraint

$$\omega_{pe}^2 < \omega_{gyro}^2 < \omega_{max}^2, \tag{21}$$

where ω_{pe} is the plasma frequency, ω_{gyro} the gyrofrequency and ω_{max} the maximum available gyrotron frequency. ω_{max} depends on the available gyrotron technology and can be set by the user as an input. The critical density is reached when the plasma frequency matches the electron cyclotron frequency. Thus, the (central) electron density n_e is limited to:

$$n_e < n_{e,crit}^{ECRH} = \frac{m_e \epsilon_0}{e^2}\omega_{gyro}^2,\ \omega_{gyro} < \omega_{max}. \tag{22}$$

Figure 3 visualizes the heatable densities with O1-heating, and in comparison X2, heating schemes with different maximal gyrotron frequencies at varying magnetic field strengths.

Equation 22 is implemented as a constraint in Process.

Note that there are heating schemes, such as Electron Bernstein Waves [29] or an X1 heating scheme, which could be used to heat a plasma beyond Equation 22, but their relevance as a heating scheme in a stellarator reactor need to be shown and are not taken into account by Process yet.

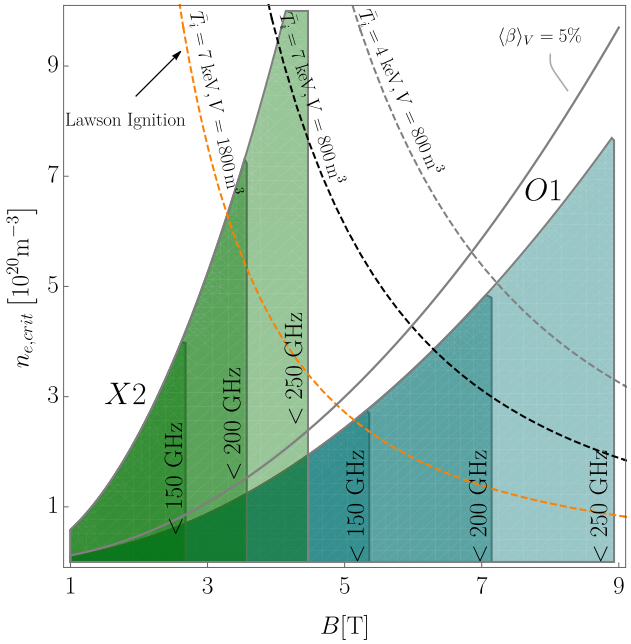

Figure 3: Central density limits due to different ECRH heating schemes: The blue regime indicates where O1 heating can be applied, the green regeion where X2 is feasible. Each shape area indicates a minimum required gyrotron frequency. Dashed lines indicate ignition according to Lawson criterion with different Volume V and volume averaged ion temperature $\bar{T}_i$ (assuming $n_{peak}/\bar{n}$=3 and ISS04 scaling from W7X parameters.)

3.5. Island Divertor

There are three studied divertor concepts available for stellarator reactors: An ergodic divertor concept, also called helical divertor, for high shear configurations [30], a resilient non-resonant divertor concept [31] and a resonant, island divertor concept [32, 33, 34, 35]. For now, we include only a description for an island divertor concept in PROCESS, closely following the (previously implemented) model as proposed in [15].

In a stellarator with an island divertor concept, the magnetic field is designed such that the rotational transform ι_{res} at the edge coincides with a low order rational number $N_p k/n$,

$$\iota_{\mathrm{res}} = \frac{kN_p}{m} \equiv \frac{n}{m}, \tag{23}$$

where m is the number of poloidal resonances (islands), k is the resonance order and N_p is the field period of the machine. k is determined by radial B-Field harmonics on or shortly behind the last closed flux surface, and, if the respective resonant harmonics are not actively suppressed, is typically equal to 1. The underlying concept of the island divertor is to use the magnetic islands for diverting the heat load coming from the plasma core and then intersect the islands with discontinuous divertor target plates. While the full physics description of the stellarator scrape-off-layer (SOL) is still a challenging and contemporary topic, fundamental geometrical considerations can be used to estimate the heat load on the divertor target plates. It is the goal of the proposed model here to provide an estimation of the peak heat load, as this is the constraining engineering limit, due to material limitations.

The heat load on the divertor target plates q_{div} is the ratio of the power arriving at the divertor P_{div} and the area over which this power is effectively spread, A_{eff}. One of the major strategies to reduce the heat load arriving at the divertor is to introduce low-Z impurities that are effective at radiating substantial power in the SOL. Consequently, the power arriving at the divertor is the power coming from the plasma core P_{core} less the radiation from the impurities: $P_{\mathrm{div}} = P_{\mathrm{core}}\,(1 - f_{\mathrm{rad}})$, where f_{rad} is the radiation fraction, which needs to be given as an external input parameter.

The wetted area A_{eff} on the divertor plates usually has the form of a strike-line with a total length L_{tot} across all divertors and a width λ_{int}. The heat load is then

$$q_{\mathrm{div}} = \frac{P_{\mathrm{div}}}{A_{\mathrm{eff}}} = \frac{P_{\mathrm{core}}\,(1 - f_{\mathrm{rad}})}{L_{\mathrm{tot}} \cdot \lambda_{\mathrm{int}}}, \tag{24}$$

where P_{core} is provided by the PROCESS' plasma core model.

Assuming that the heat load is distributed in equal shares across all divertor plates, then the total length L_{tot} is simply the sum over all divertor targets L_i,

$$L_{\text{tot}} = \sum_i L_i = 2nL_{\text{strike}}. \tag{25}$$

Here $n = k\,N_p$, as defined previously. The strike-line length L_{strike} on a single divertor plate can be estimated from the field line geometry. To this end, one needs to introduce the pitch-angle $\Theta = dr/dl$, which describes the radial displacement of a field line in the SOL along its arc-length and depends on the specific magnetic configuration $\mathfrak{C}$, but it is typically in the range of 10^{-3} – 10^{-4} for stellarators. The strike-line is limited by the field line that just passes the divertor plate at the front and then after one toroidal turn ($\Delta l \approx 2\pi R$) hits the target plate on the far side. Using the definition of the pitch-angle, the radial projection of the strike-line is $\Delta r = 2\pi R\Theta$. The length of the strike-line on the divertor plate itself is then determined by the angle $\alpha_{\text{lim}} = \Delta r / L_{\text{strike}}$ under which the field line hits the target plate. The strike-line length on the divertor is then simply

$$L_{\text{strike}} = 2\pi R \frac{\Theta}{\alpha_{\text{lim}}} F_x, \tag{26}$$

where F_x is an additional broadening of the flux channel caused by diffusive cross-field transport. A model for this factor is given below in Equation 30.
A small intersection angle α_{lim} helps to increase the strike-line length and reduce the heat load density. However, α_{lim} is limited by the engineering accuracy under which target elements can be arranged: typically around $\sim 2°$.

Generally, stellarators with an island divertor feature much longer connection lengths than tokamaks [36]. Consequently, the energy and particles have a longer dwell time in the SOL leading to a substantial cross-field broadening of the transport channel compared with tokamaks. We assume here that the cross-field transport is mostly of diffusive nature, allowing us to describe the strike-line width (also referred to as power decay width) by [37],

$$\lambda_{\text{int}} = \sqrt{\chi_\perp \cdot \tau_\parallel}. \tag{27}$$

Here, $\chi_\perp$ is the perpendicular diffusion coefficient, which is an user-defined
input, but usually taken in the order of $\sim 1\,\text{m}^2/\text{s}$ [38]. $\tau_\parallel$ is the characteristic

dwell time of the particles in the SOL before reaching the target. As the particles follow the field lines, the dwell time $\tau_\parallel$ depends on the connection length L_c of the field line and the average speed of the particle, namely the ion sound speed $c_s = \sqrt{2T/m}$ (m here being the ion mass), and thus $\tau_\parallel = L_c/c_s$. The ion temperature (in the SOL) T is again a user-defined input, however since mostly detached scenarios are considered for a reactor design point for divertor protection, T must be on the order of 5 – 10 eV.

The connection length L_c can be geometrically estimated by using again the definition of the pitch-angle Θ. If we define Δ as the radial distance from the LCFS to the target plate, then the connection length is simply

$$L_c = \frac{\Delta}{\Theta} = f \cdot \frac{w_i}{\Theta}. \tag{28}$$

The typical radial scale length Δ of the system is for the island divertor the radial extent of the magnetic islands w_i. However, as the island is intersected by the divertor plates, only a fraction f of the island width is effectively used $\Delta = f \cdot w_i$. Usually, the divertor plates are placed at the half radius of the islands, thus f is normally on the order of $f \sim 0.5$. The full width of the island can be estimated from analytic theory [39],

$$w_i \approx 4 \cdot \sqrt{\frac{R \cdot \Theta}{m \cdot \iota'}}, \tag{29}$$

where $\iota' = d\iota/dr$ is the magnetic shear at the edge, which is given by the magnetic configuration. Generally, stellarators with an island divertor need a comparably low magnetic shear in order to form sufficiently large magnetic islands.

Finally, the previously mentioned flux channel broadening F_x can be derived following the same diffusive ansatz, but for only one toroidal turn, which then becomes:

$$F_x = 1 + \frac{1}{\Theta}\sqrt{\frac{\chi_\perp}{c_s 2\pi R}}. \tag{30}$$

In conclusion, we have provided equations for all introduced parameters. Consequently, all the here derived relations can be consolidated in order to arrive at a heuristic scaling for the divertor heat load

$$q_{\mathrm{div}} = \frac{P_{\mathrm{core}}\,(1 - f_{\mathrm{rad}})}{8\pi R k N_p F_x} \cdot \frac{\alpha_{\mathrm{lim}}}{\Theta} \cdot \sqrt{\frac{c_s}{f \cdot \chi_\perp}} \sqrt[4]{\frac{k N_p \iota' \Theta}{\iota R}}. \tag{31}$$

The device specific parameters $\iota(\mathfrak{C})$, $\iota'(\mathfrak{C})$, $N_p(\mathfrak{C})$,$k(\mathfrak{C})$ and $\Theta(\mathfrak{C})$ are specific to the considered magnetic configuration and are easily obtained in the pre-processing step. $\chi_\perp$, α_{lim}, and T depend on the specific physics regime and engineering accuracy and must be provided by the user, but usually take values as indicated in the text above.

It is planned to validate this model against experimental results from Wendelstein 7-X in the future. Due to the analytic nature of the model, it will be possible to quickly adapt and test new findings and advances.

It should also be noted, since the heat load is usually limited by material constraints, the divertor model is also useful in reversing the parameters. For example, for a fixed design point and heat load limit, one can estimate the required radiation fraction that would be needed to make the design point feasible.

3.6. Blanket

We base the stellarator description of the tritium breeding blanket on PROCESS' 1D helium cooled pebble bed (HCPB) blanket model for tokamaks [40].

We expect this model to hold reasonably well also for stellarator devices. An important feature for stellarator reactors however is an inhomogeneity of neutron loads of the first wall in toroidal direction. This can be encountered for when introducing a neutron peaking factor f_{peak} in the model, which measures the inhomogeneity of the neutron load along the blanket area. For a given configuration, this factor can be calculated by

$$f_{peak}(\mathfrak{C}) \equiv \left.\frac{q_{max}}{q_{\text{avg}}}\right|_{\text{ref}}. \tag{32}$$

q_{max} is the maximum and q_{avg} the average neutron load on a two dimensional hyper-surface between plasma and coils at a reference design point. We calculate the wall load q in the pre-processing step by using a simple $1/r^2$ decay of the neutron intensity. When one constructs an intermediate, first wall like, hyper-surface between plasma and coils, one can calculate q on this surface via

$$q(\theta,\phi) = \frac{E_n}{4\pi}\int_{V_S} d\mathbf{x}_S \frac{\hat{\mathbf{n}}(\theta,\phi)\cdot(\mathbf{x}_S - \mathbf{x}_W(\theta,\phi))}{||\mathbf{x}_S - \mathbf{x}_W(\theta,\phi)||^3} f_S(\mathbf{x}_S). \tag{33}$$

Here, θ and ϕ are poloidal and toroidal coordinates on the surface, $\mathbf{x}_S$ and $\mathbf{x}_W$ are the position vectors of the source and the wall respectively, V_S stands for the volume of the source and $\hat{\mathbf{n}}$ is the normal vector of the wall. E_n is the energy carried by a neutron in a $D+T$ reaction (14.1 MeV). f_S is the neutron fluence at the source point $\mathbf{x}_S$, which can be obtained using the Bosch-Hale fit[41] for a reference density and temperature profile:

$$f_s \equiv n_D n_T \langle\sigma v\rangle = C_1 n_D n_T \theta(T)\sqrt{\frac{\xi(T)}{m_r c^2 T^3}} e^{-3\xi(T)} \tag{34}$$

θ, ξ are fit functions and C_1 is a fit parameter, see [41] for their explicit form. An example calculation of Equation 33 for a wall in a HELIAS 5 device is shown in Figure 4.

Equation 33 simplifies the geometry vessel by neglecting 'shadowed' regions in the vacuum vessel and it further does not account for neutron scattering, but is a method to compute the peaking factor computationally fast.

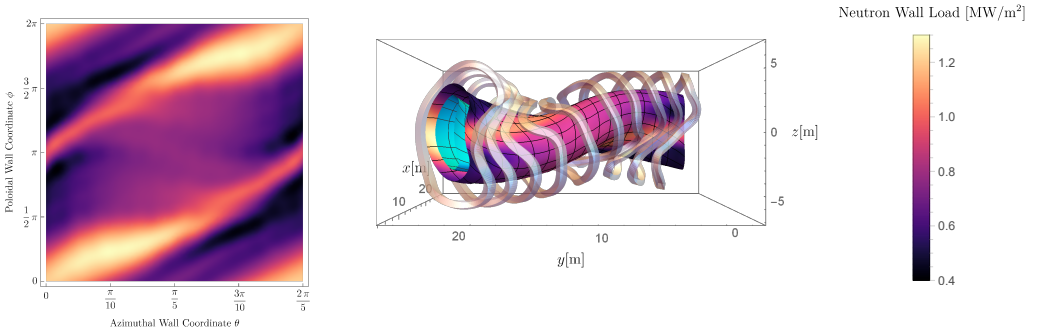

Figure 4: An example calculation of the neutron flux for a HELIAS 5 configuration on a conceptional intermediate hyper surface between wall and coils using Equation 33 at 3 GW fusion power. Left: The flat projection of $q(\theta, \phi)$ in one module. Right: The neutron wall load on the imposed hypersurface. The last closed flux surface is shown in cyan.

More sophisticated values for f_{peak} can be obtained by dedicated 3D Monte-Carlo codes such as MCNP [42], which can include neutron scattering and further are able to resolve in detailed vessel and blanket geometries at the cost of computational time. Equation 33 can be substituted with results from an MCNP run in PROCESS, if more accuracy is needed.

3.7. Stellarator Coils

For a given toroidal magnetic field strength B_t on axis, PROCESS should calculate the required coil current in the pre-defined coil filaments. This is achieved by using a simple linear scaling from a pre-calculated value for the averaged norm of the toroidal field on axis, $\langle B_t \rangle_{axis}$. Once determined for a reference point, the scaling of the coil current with respect to B_t and R is of course linear,

A systems code must self-consistently calculate the required coil current for a given toroidal magnetic field strength $B_t \equiv \langle \hat{B}_t \rangle_{axis}$.

In PROCESS total coil current I is obtained for any value of B_t and R by a simple linear scaling

$$I = I_0(\mathfrak{C}) \frac{\langle B_t \rangle}{\langle \hat{B}_t \rangle} \frac{R}{\hat{R}}. \tag{35}$$

The needed coil current $I_0(\mathfrak{C})$ for the respective B_t at the reference design point can be calculated using the Biot-Savart equation, which is done

numerically in the pre-processing step. The (vacuum) axis can be obtain by a field line tracer, e.g. [43], or as output by the equilbrium code VMEC.

Another important parameter for the coil design in a systems code is the maximum magnetic field on the coil surface B_{max}, which is crucial for the superconductor material constraints. B_{max}, however, needs a more sophisticated treatment, as it depends on the coil cross-section area. For the calculation of the magnetic field on the coils B_{max} at the reference design point with $\hat{R}$, $\hat{B}$, and the winding pack thickness $\hat{A}_{WP}$ we proceed as follows.

For stellarators, we approximate the winding pack to be of rectangular shape and homogeneously filled with a current carrying material. With these assumptions, Biot-Savarts volume integral can be in good approximation reduced to a Riemann sum of analytically solvable integrals of the magnetic field due to homogeneously filled straight cuboid beams [44, 45], as we derive again in Appendix A. For reasonable accuracies, each coil is discretised into $\mathcal{O}(100)$ straight beams, each producing a magnetic field $\mathbf{B}_i^{\text{Beam}}$ at position $(\mathbf{x})$. The total contribution of a coil to the magnetic field at a position $(\mathbf{x})$ can then be approximated by

$$\mathbf{B}_{\text{coil}}(\mathbf{x}) \simeq \sum_i \mathbf{B}_i^{\text{Beam}}(\mathbf{x}). \tag{36}$$

The derivation and an explicit formula for $\mathbf{B}_i^{\text{Beam}}$ is given in Appendix A. B_{max} then becomes

$$B_{max} = \max_{\mathbf{x}} \sum_{coils} \mathbf{B}_{\text{coil}}(\mathbf{x}). \tag{37}$$

This descriptions allows an, for our purposes, accurate calculation of the magnetic field at the surface of the coils and in the current carrying material. The latter will be important for the force calculations that will be introduced in the next section.

The scaling within the systems code needs to reflect that B_{max} depends on the winding pack cross-section. Therefore, we calculate Equation 37 for varying winding pack sizes in the pre-processing step.

B_{max} can then be simply parametrized in PROCESS via a fit function, which we choose here in the form of

$$B_{max}(A_{wp}) = \frac{\mu_0 I N}{R - a_{coil}} \left(a_0(\mathfrak{C}) + \frac{R}{\sqrt{A_{wp}}} a_1(\mathfrak{C}) \right). \tag{38}$$

The first summand approximates the ideal part (due to an ideal Toroid), the second summand includes the fitted scaling with changing winding pack size. a_{coil} is the average minor coil radius, N the number of coils, and A_{wp} the cross-sectional area of the winding pack. a_0 and a_1 are fit parameters that are obtained in the pre-processing step by varying $\hat{A}_{wp}$ using Equation 37.

Another stellarator-specific output parameter of the coil module is the maximal curvature in the coils. This parameter is especially relevant for stellarators as the non-planar coils can have small bending radii that might not be in line with limitations imposed by the superconductor material. Again, the maximal curvature can be obtained through a scaling equation, when a reference value has been obtained in the pre-processing step

$$\kappa_{\max} = \frac{R}{\hat{R}} \frac{1}{1 - \frac{d_{WP}}{2a_{Coil}}} \kappa_{\max}(\mathfrak{C}). \tag{39}$$

Here, d_{WP} is the radial thickness of the winding pack and a_{coil} the average minor coil radius. The reference value for the maximal curvature $\kappa_{max}(\mathfrak{C})$ is calculated in the pre-processing step according to

$$\kappa_{max} = \max_{\theta,i} \frac{\|\gamma_i'(\theta) \times \gamma_i''(\theta)\|}{\|\gamma_i'(\theta)\|^3}, \tag{40}$$

where $\gamma_i : I \subset \mathbb{R} \to \mathbb{R}^3$ parametrizes the i-th coil in the set and θ is a local coil coordinate.

The electromagnetic forces that act on the coils are important because the integrity of the structural material is limited by the stress, which again scales with the force magnitude. This fact is especially limiting for compact devices at higher magnetic field, as those typically imply high operating current densities resulting in high forces. The force density, as the other parameters before, is calculated for a reference coil size and then scaled within PROCESS. For this purpose, the magnetic field $\mathbf{B}$ is calculated *inside* the winding pack, using the finite winding pack Biot-Savart approximation introduced in Equation 36. The Lorentz force density at a point $\mathbf{x}$ in the winding pack is then simply

$$\mathbf{f}(\mathbf{x}) = \mathbf{B}(\mathbf{x}) \times \mathbf{j}(\mathbf{x}) = j \, (\mathbf{B}(\mathbf{x}) \times \mathbf{t}(\mathbf{x})) \,, \tag{41}$$

if the magnitude of $\mathbf{j}$, the current density, is assumed to be constant and homogenous across the coil cross section and points along the tangential

direction $\mathbf{t}$ of the coil. Figure 5 shows an example calculation of the force density distribution in a stellarator coil: In every poloidal cross section of the coil we discretize the winding pack cross-section into $N \times N$ volume elements dV for which we calculate a force density $\mathbf{f}$ using Equation 41. $\mathbf{f}$ can be integrated over A_{wp} to obtain a force density $\bar{f}$ in N/m, or over the whole coil volume V_{coil} to obtain a force F in N. $\max f$ needs to be held by the structural material in the winding pack, $\bar{f}$ result in coil jacket and coil insulation stresses and F is relevant for the outer coil support structure.

We calculate the effective parameter as the maximum of each of these forces according to $f_{max}(\mathfrak{C}) \equiv \max_{\theta,i} |\mathbf{f}|$ (θ a poloidal coil coordinate, i indicates the coil number) for every configuration and scale it in PROCESS according to

$$f_{max} = f_{max}(\mathfrak{C}) \frac{j}{\hat{j}} \frac{B_{max}}{\hat{B}_{max}}, \tag{42}$$

$$\bar{f}_{max} = \bar{f}_{max}(\mathfrak{C}) \frac{I}{\hat{I}} \frac{B_{max}}{\hat{B}_{max}}, \tag{43}$$

$$F_{max} = F_{max}(\mathfrak{C}) \frac{I}{\hat{I}} \frac{B_{max}}{\hat{B}_{max}} \frac{\ell_{coil}}{\hat{\ell}_{coil}}. \tag{44}$$

Here, j is the current density, I the coil current, ℓ the length of the respective coil (in PROCESS). Hatted values again denote the values at the reference point where $f_{max}(\mathfrak{C})$, $\bar{f}_{max}(\mathfrak{C})$ and $F_{max}(\mathfrak{C})$ are calculated.

It should be noted that one needs to make an assumption about the orientation of the winding pack in order to calculate the force density. To this end we choose the normal vectors of the winding pack to point into the (cylindrical) toroidal and radial direction respectively. In a winding pack, which is optimized with respect to torsion and stresses, this normal vector might deviate from this assumption, however, f_{max} will not be affected significantly by this choice.

As stellarators can have significant lateral forces, PROCESS also returns lateral and radial projections of Equation 41 which are scaled analogously to Equation 43. Figure 6 shows the order of magnitude of lateral projection of $\bar{f}$ in a HELIAS 5 coil set.

To estimate the stress on the ground insulation of a coil set we use a simple model and only consider normal uniaxial stresses which depend on

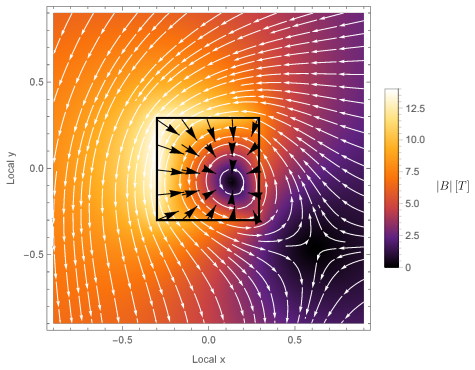

Figure 5: Cross section through a quadratic winding pack of dimensions 60 cm in a high field region of a stellarator coil. The cross section homogeneously carries a current of 14 MA (produces 5.6 T in a HELIAS 5 configuration). Colour coded is the absolute magnetic field strength. Axes are set in local coordinates. Black arrows indicate directions and magnitude of local forces in the winding pack.

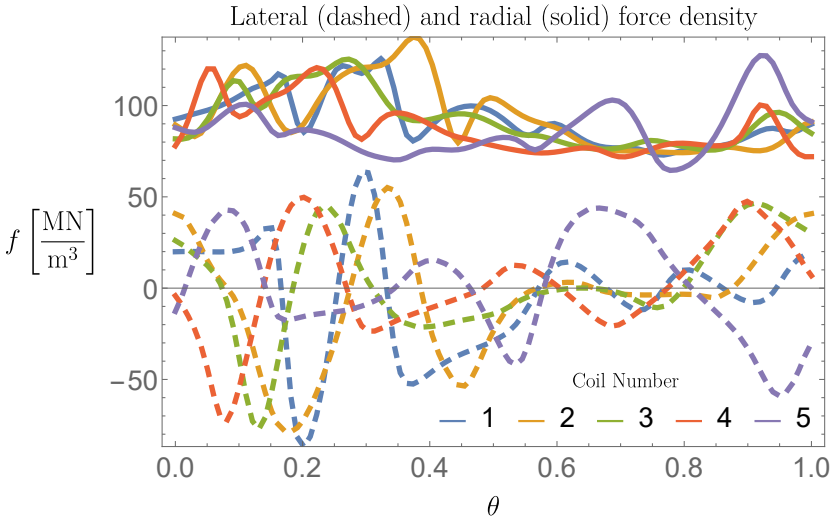

Figure 6: The magnitude of the radial and lateral force density on the nonplanar coils in one half-module of a HELIAS 5-B coil set [46] with 5.6 T on axis and 22m outer radius. θ is a periodic poloidal coil coordinate. Maximum absolute values for radial and lateral projections are taken as effective parameters.

the poloidal coil coordinate θ, namely

$$\sigma_{\text{insulation}}(\theta) = \frac{||\mathbf{F}(\theta)||}{A}. \tag{45}$$

We assume that the forces $\mathbf{F}(\theta)$ point orthogonal towards the outer boundary of the coil and thus create a pressure on the radially outward area of the coil A, which depends on the winding pack size. Assuming a fixed outer coil boundary condition, the maximal stress on this area, induced by the winding pack forces, then is

$$\sigma_{max} \simeq f_{max}\, d_{WP}, \tag{46}$$

where d_{WP} is the radial thickness of the winding pack as calculated by PROCESS from Equation 47.

This stress is subject to the elastic limit of the material under pressure. If a coil design as in [46] is assumed, the stress on the ground insulation and its upper limit will be on the order of ~ 200 MPa. In our implementation, the maximum allowable stress is a user defined parameter and if set, PROCESS will optimize the design to fulfill this constraint.

It should be noted that we ignore stresses in the coil structural material for now, as accurate values for the peak stresses would require a detailed design of the coil support structure. Possibly, some simplifications of the support structure could be made, like a thin massive inter-coil shell, which could provide an idea about stresses in the coil support structure with the help of finite element calculations, but this is beyond the scope of this paper.

3.8. Winding Pack Design

For tokamaks, PROCESS is capable of optimizing the winding pack constituents (copper and superconductor fractions) with respect to the figure of merit. In [16] this degree of freedom was not implemented for stellarators, which we now enable using the following prescription.

For the stellarator version of PROCESS, we model the winding pack with N squared turns, surrounded by a coil jacket and some user defined ground insulation thickness on this coil jacket. Each of the N turns has a composition as shown in Figure 7. The inner part of the conduit contains an approximate squared conductor area. The structure and helium fraction as well as the insulation thickness in the conduit cross section are user defined parameters, whose values are subject external specifications. Especially the

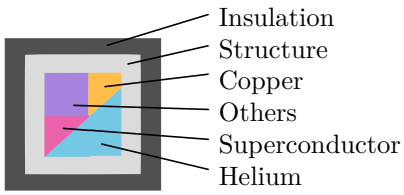

Figure 7: The used winding pack architecture of one turn. The whole winding pack consists of N such turns. The shown fractions are not for scale.

fraction for the structural material needs to match the inner winding pack stress constraints, which are non-trivial in 3D coils and demand a sophisticated treatment. The copper- and superconductor fractions, in contrast, are subject to quench protection and can be calculated by PROCESS, as will be addressed later in this section. The overall dimension of the turn area is a user defined parameter.

For stellarator coils, PROCESS now optimizes the copper and the superconductor fractions according to the consistency equation

$$\frac{I}{A_{wp}\, f_{\mathrm{scu}}} \stackrel{!}{=} f_j\, j_{crit}\Big(B_{max}(A_{wp}), T, \epsilon\Big). \tag{47}$$

Here, $f_j \leq 1$, is an iteration parameter and is bounded by user defined values. j_{crit} is a parametric form for the critical current density of the superconductor which depends on T, the temperature in the superconductor, $B_{max}(A_{wp})$ as given from Equation 38 and ϵ the maximal strain in the superconductor. Currently, the implemented superconductor material parametrizations in PROCESS cover Nb_3Sn, NbTi, Bi-2212 and a REBCO-Material [20].

The superconductor fraction f_{scu} in the winding pack is a resulting parameter from the winding pack material area fractions,

$$f_{scu} = \underbrace{(1 - f_{case})}_{\text{conduit fraction}} \quad \underbrace{(1 - f_{He})}_{\text{conductor fraction}} \quad \underbrace{(1 - f_{Cu} - f_{oth})}_{\text{SC fraction}}, \tag{48}$$

where f_{case} is the case and insulation fraction of the whole *turn area*, f_{He} is the helium fraction in the *conduit area* and f_{Cu} and f_{oth} are copper and other material fractions in the *conductor area*. PROCESS finds the appropriate winding pack dimensions then by solving Equation 47 for A_{wp}, which is a simple root finding problem and is solved by Newton's method within PROCESS. In Equation 48, f_{Cu} is an iteration parameter in PROCESS and is bounded by quench protection arguments, which we will address below.

In the case of a quench, the internal TF coil current needs to be dumped into external resistors. The exponential decay time of the coil current during the quench is parametrized in PROCESS by τ_Q. This value is an iteration parameter, subject to the constraints:

1. Maximum voltage in the TF coils (lower boundary)
2. Temperature rise in the TF coils (upper boundary)
3. Stress on the vacuum vessel by eddy currents (lower boundary)

The first constraint restricts τ_Q by the maximal allowable voltage across a coil and during a quench which is, for large resistances, approximately given by [20]

$$U = 2\,\frac{E_{stoTF}}{\tau_Q I} = \frac{LI}{\tau_Q N_{TF}}. \tag{49}$$

E_{stoTF} is the approximative average stored energy per coil, L the inductance of the coil set, N_{TF} the number of coils, and I is the average coil current. The inductance of a stellarator coil set is calculated in the pre-processing step (e.g. by assuming a filamentary 3D curve approximation of the coils [47, 48]) for a reference point and can be scaled in PROCESS according to

$$L = L(\mathfrak{C})\frac{a_{coil}^2}{\hat{a_{coil}}^2}\frac{\hat{R}}{R}. \tag{50}$$

This equation is based on an ideal toroid, where a_{coil} is the minor average coil radius. The restriction for τ_Q is then

$$\tau_Q > \frac{LI}{U_{max} N_{TF}}. \tag{51}$$

The second constraint for τ_Q due to the temperature rise during a quench can be quantified using an energy conservation argument leading to

$$J_{WP} < (1 - f_{case}) \sqrt{\frac{2}{\tau_{dump}\eta}\Big(f_{Cu}^2 f_{cond}^2 q_{cu} + f_{Cu} f_{cond}(1 - f_{cond}) q_{He} + f_{Cu} f_{cond}^2 (1 - f_{Cu}) q_{scu}\Big)}. \tag{52}$$

In Appendix B we provide a short derivation of this equation.

Finally, the third constraint considers the fact that the changing current in the coils during a quench induces a stress in the vacuum vessel. The maximum allowable force density in the vacuum vessel during a quench f_{VV} puts another lower bound on τ_Q. We use a scaling equation to calculate the maximum force density based on a reference value according to

$$f_{\mathrm{VV}} = f_{\mathrm{VV}}^{(ref)} \left(\frac{d_{\mathrm{VV}}\, \tau_Q\, R_{\mathrm{VV}}}{B I a^2} \right)_{\mathrm{ref}} \frac{B I a^2}{d_{\mathrm{VV}} \tau_Q R_{\mathrm{VV}}}, \tag{53}$$

where the reference values can be a user defined input.

For now, we choose a sophisticated ANSYS simulation from W7-X as a reference value as illustrated in Figure 8, where 2.54 $\mathrm{MN/m^3}$ is the maximum value of the force density. Note that this step is not done in every pre-processing step, but instead is only provided once for the W7-X vacuum vessel. We assume for now that, in first approximation, this value also reflects the general inhomogeneity for any type of stellarator vacuum vessel. However, the reference value can be easily adapted for designs where more detailed simulation results exist. With values from W7-X, Equation 53 becomes

$$f_{\mathrm{VV}} \simeq \left(9.3 \cdot 10^{-2}\, \frac{\mathrm{s}}{\mathrm{m}^2} \right) \cdot \frac{B\, I\, a^2}{d_{\mathrm{VV}}\, \tau_Q\, R_{\mathrm{VV}}} \tag{54}$$

Also note that this constraint could in principle be overcome by a poloidal electric break, e.g. [49]. In PROCESS f_{VV} is then bound to a user defined parameter and serves as an inequality constraint.

3.9. Structure Mass

As shown in the previous section, large lateral forces can act on the non-planar stellarator coils. However, the details of the force distribution depend very much on the coil shapes and winding pack. This puts not only great demands on the support structure, but also makes it difficult to design an appropriate structure. Consequently, such designs for large stellarators are scarce. There exist only a few design concepts for a stellarator reactor, such as a bolted or welded plates [18] or support elements with 'stiffeners' [50].

Instead of implementing a specific design in PROCESS, we choose to model only the total structure mass while not being sensitive to the details of support structure. The total mass is a good proxy, both, for the cost and the

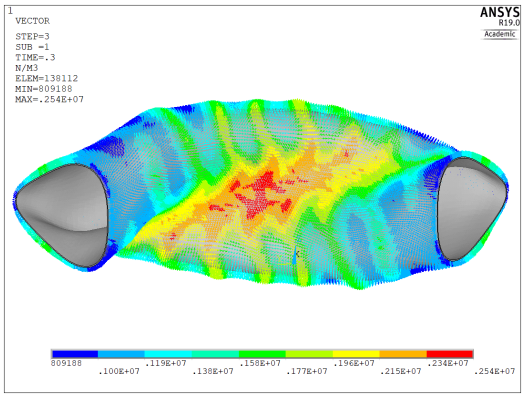

Figure 8: ANSYS calculation of the force densities in the W7-X vacuum vessel without ports. Peak value is $2.54 \cdot 10^6$ N/m^3, by Jiawu Zhu.

complexity of the support structure. As introduced already in [15], we stick here to an empirical scaling law as described in [51] to calculate the structure mass in PROCESS,

$$M_{struct} = 1.348\, W_{mag}^{0.78}. \tag{55}$$

Although Equation 55 sees good empirical agreement, it does not show whether the design point has local unsupportable forces. In reality, the optimisation of the support structure is a difficult task to ensure the integrity of the device while avoiding local overloads.

3.10. Build consistency and port sizes

Scaling in R and the winding pack requires that PROCESS checks the inner coil-coil distances in toroidal direction to prevent that coils come too close in azimuthal direction. We incorporate this constraint via an effective parameter of the minimal distance between two central filaments $d_{min}(\mathfrak{C})$, which is calculated in the pre-processing step. This distance scales linearly with the major radius and is subject to the constraint

$$d_{min}(\mathfrak{C})\,\frac{R}{\hat{R}} > w_{WP} + w_{case}, \tag{56}$$

where w_{WP} denotes the toroidal width of the winding pack as calculated by the routine described in subsection 3.8 and w_{case} is the implied coil casing width in toroidal direction.

Furthermore, the radial distance between the plasma and the coils is also subject to build constraints. For stellarators, the most critical location is the point where the coils come closest to the plasma. One value for this distance at a reference device size is calculated in the pre-processing step and defines an effective value as $d_{pc}(\mathfrak{C})$. In PROCESS we then implement the scaling:

$$d_{pc} = \frac{R}{\hat{R}} \left(f_{geo}(\mathfrak{C})\, \hat{a} \left(\frac{\hat{A}}{A} - 1 \right) + d_{pc}(\mathfrak{C}) \right). \tag{57}$$

Here, $f_{geo} = \frac{\partial d_{pc}}{\partial a}$ accounts for how much the plasma wall distance changes when decreasing the minor radius in the same configuration. A is the (scaled) aspect ratio and $\hat{A}$ the aspect ratio at the reference point.

In PROCESS, d_{pc} is then subject to the constraint

$$d_{pc} > \frac{d_{coil}}{2} + d_{VV} + d_{shield} + d_{blanket} + d_{fw} + d_{SOL} + g_{ap}, \tag{58}$$

where d_{coil} is the radial thickness of the coil (winding pack plus coil jacket and insulation), d_{VV} is the thickness of the vacuum vessel, d_{shield} of the thermal shield, $d_{blanket}$ the thickness of the blanket, d_{fw} the thickness of the first wall and d_{SOL} describes the width of the scrape-off layer. g_{ap} accounts for the left available space.

Note that by this prescription PROCESS only ensures radial build consistency along one line in the stellarator geometry and in general the gap is a function of a poloidal and toroidal angle, $g_{ap} = g_{ap}(\phi, \theta)$. Equation 58 is implemented via a stellarator specific inequality constraint in PROCESS.

Finally, we calculate a maximal rectangular vertical port size area $A^{max}_{Port}(\mathfrak{C})$ in the pre-processing step for a reference point. Each dimension is then scaled linearly with the major radius within PROCESS. The maximum port size limits the maximum size of blanket segments and is thus an important information to judge the feasibility of remote maintenance.

3.11. Concluding remarks

We listed the implemented changes in which PROCESS' prescriptions of a stellarator power plants now differs from the tokamak prescription. For this, we identified important reactor relevant stellarator-specific features and implemented them to sufficient accuracy in PROCESS using an additional pre-calculation step. However, there are more stellarator specific constraints in a power plant which are not included yet. For example, alpha particle damage

on the wall and inhomogeneous radiation loads are approximated by the (axi-symmetric) description of PROCESS. Proper stress and strain calculations for stellarator devices are ignored for now in PROCESS. Capturing these modifications require more detailed calculations and stellarator design studies and need to be added in future publications.

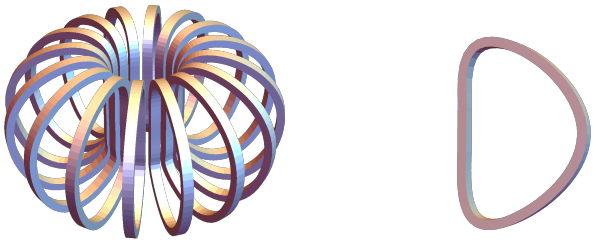

Figure 9: The used tokamak DEMO TF-coil set for the comparison (output of tokamak-PROCESS). The winding pack cross section shape is simplified as rectangular in stellarator-PROCESS.

4. Application

In this section we apply the modified PROCESS code to three different stellarator-specific scenarios: First, we carry out a benchmark of the newly developed stellarator coil module against the (established) tokamak coil module. Secondly, we apply for the first time PROCESS to three distinct stellarator configurations with different aspect ratios. This is possible only due to the newly developed models. Thirdly, we use PROCESS to compare three different stellarator coil-sets for the same magnetic configuration to demonstrate the capability of checking coil sets for their feasibility.

4.1. Tokamak PROCESS Benchmark

The stellarator models were designed to accommodate any type of stellarator. This flexibility allows to model also a tokamak-coilset within the stellarator-PROCESS version.

In this section, we briefly benchmark the results of the new stellarator coil module in PROCESS against the output of a tokamak-PROCESS DEMO run, starting from 16 D-shaped coils as shown in Figure 9. The coil shapes for the stellarator-PROCESS run are produced by tokamak-PROCESS and are taken as input for the stellarator run.

We obtain effective parameters $a_i(\mathfrak{C})$ for the tokamak coil set in the preprocessing step as described in the previous section and then run stellarator-PROCESS in optimization mode, optimizing for cost of electricity. We fix the magnetic field strength on axis to 5.72 T and the aspect ratio to 3.1 and

Description	PROCESS	sPROCESS
Toroidal magnetic field strength [T]	5.72	5.72*
Aspect Ratio [1]	3.10	3.10*
Maximal Field on the coils [T]	13.2	12.7
Stored Magnetic Energy [GJ]	182	170
Total Coil Current [MA]	256	255
WP Current Density [MA/m^2]	1.49×10^7	1.64×10^7
j_{op}/j_{crit} [1]	0.597	0.600
Superconductor Mass per Coil [kg]	2.14×10^4	2.52×10^4
Copper Mass per Coil [kg]	1.54×10^5	1.46×10^5
WP Steel Mass per Coil [kg]	1.68×10^5	1.68×10^5
Max. Force Density [MN/m^2]	98.2	102
WP toroidal thickness [m]	1.18	1.12
WP radial thickness [m]	0.904	0.861
Quench dumping time [s]	76.5	75.0*
Max. Quench Voltage [kV]	3.73	3.72
WP Copper fraction [1]	0.851	0.854

Table 1: Output comparison of the independently implemented coil modules of tokamak and stellarator-PROCESS using a tokamak-DEMO design. Starred values are input parameters for stellarator-PROCESS (sPROCESS). 'WP' in the descriptions abbreviates the "coil winding pack".

let PROCESS find a consistent design point while optimizing for engineering parameters, such as the copper fraction of the conductor, the winding pack dimensions, and the exponential coil quench dump time.

The result of the benchmark is displayed in Table 1. Stellarator-PROCESS converges to a similar design point as the tokamak-PROCESS version. The winding pack dimensions and the copper fraction is optimized to similar values. The maximal magnetic field on the coils deviates by 5%, which is within the model accuracy.

In the parameters shown, the calculations for the maximal magnetic field is different for tokamak and stellarator-Process, the inductance (and thus the magnetic energy) is calculated by two different models, the winding pack constituent model is implemented separately, the quench routine is seperate and the coil currents are separately calculated, too.

Generally, we find very good agreement of our stellarator coil model with the tokamak case, providing confidence in the developed model.

4.2. PROCESS for stellarators with different aspect ratios

Using the new stellarator prescription, PROCESS can now be used to model different stellarator power plants with distinct plasma equilibria and their associated coil sets. To demonstrate this, we apply PROCESS to three optimized stellarator devices with different aspect ratios and number of field periods: HELIAS 3, HELIAS 4 and HELIAS 5, see Figure 10. These designs have a field periodicity of 3, 4, and 5 respectively, as described in [52]. For each coil-set we calculate a vacuum VMEC free boundary equilibrium and determine the effective parameters as described in the previous section.

We then run PROCESS in optimization mode where we optimize for capital costs and vary the following parameters: The overall temperature and the overall density (for fixed profile shapes, α_T=1.2, α_n=0.35) as defined in Equation 13, the aspect ratio to larger values compared to the reference point, the major plasma radius, the overall magnetic field strength, and the ISS04 proportionality factor (the factor that measures how good the plasma performs with respect to the ISS04 scaling). In addition, PROCESS optimizes for winding pack dimensions and material fractions, subject to quench restrictions as described in subsection 3.8.

For every configuration we assume that 90% of the fusion alpha particles heat the plasma, which is not consistent with the considered designs, but rather needs to be seen as a target value for future stellarator reactor designs. Improved alpha particle confinement in stellarators is only recently addressed in stellarator optimization, but with promising results already [53, 54].

We then run PROCESS for an ignited power plant design point with $\sim$ 1000 MW net electricity output, which corresponds to roughly 3 GW fusion power, imposed as a constraint equation in PROCESS. We assume an ECRH heated ignition point using the prescription in subsection 3.4, with maximal available gyrotron frequencies of 200 GHz. The ISS04 transport model as in subsection 3.2 is assumed. The superconductor is taken as Nb_3Sn at 4.75 K operation temperature. The current density we limit to 80% of the critical superconducting density. Superconductor strain is neglected for the critical current density. All devices assume an island divertor and 85% radiation fraction in the scrape-off-layer. Radiating plasma impurities are neglected.

Important output parameters of the converged design points are shown in Table 2. The aspect ratios were found at greater values compared to the reference values. This indicates that the major radius of all designs is limited by the coil-plasma distance which would need to be enlarged for more economically feasible design points. This again could be possible by re-optimizing

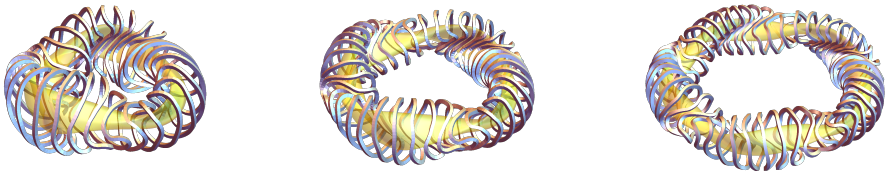

(a) HELIAS 3 (b) HELIAS 4 (c) HELIAS 5

Figure 10: The coilset and plasma boundary of the three used HELIAS configurations as described in the text.

a stellarator coil-set further away from the plasma. The study in [52] used NbTi superconductor, which we replaced by Nb_3Sn superconductors here. This allows higher field strengths of 6 to 7 Tesla on axis. The possibility to switch superconductor material also demonstrates the advantage of technological flexibility of the systems code framework.

Description	Helias 3	Helias 4	Helias 5
Plasma Beta [1]	0.0441	0.0471	0.0410
Net Electricity Output [MW]	1020	999	1020
Fusion Power [MW]	2890	2950	3070
Major Plasma Radius [m]	13.4	17.6	19.3
Minor Plasma Radius [m]	1.72	1.49	1.21
Aspect Ratio [1]	7.77	11.9	15.9
Plasma Volume [m^3]	783	769	555
Peak el. Density [$1/m^3$]	3.72×10^{20}	3.61×10^{20}	4.54×10^{20}
Peak el. Temperature [keV]	15.4	16.1	15.4
ISS04 Confinement Factor [1]	1.00	1.20	1.20
Number of tor. Field Coils [1]	30.0	40.0	50.0
Tor. B-field [T]	6.18	6.04	7.13
Max. Field on the coils [T]	13.9	13.2	12.7
Stored Magnetic Energy [GJ]	128	121	123
Total Coil Current [MA]	455	570	717
WP Current Density [MA/m^2]	2.41×10^7	2.57×10^7	2.57×10^7
j_{op}/j_{crit} [1]	0.800	0.800	0.800
Superconductor Mass per Coil [kg]	1.98×10^4	1.33×10^4	9510
Copper Mass per Coil [kg]	7.06×10^4	5.56×10^4	4.67×10^4
WP Steel Mass [kg]	7.58×10^4	5.78×10^4	4.71×10^4
Tot. Coil Mass [kg]	6.93×10^6	7.18×10^6	7.31×10^6
Structure Mass [kg]	1.33×10^7	1.27×10^7	1.29×10^7
Total Cooled Mass [kg]	2.55×10^7	2.64×10^7	2.64×10^7
Max. Force Density [MN/m]	91.3	79.8	78.5
WP toroidal thickness [m]	0.723	0.680	0.682
WP radial thickness [m]	0.868	0.816	0.819
Quench dumping time [s]	35.2	33.1	34.9
Max. Quench Voltage [kV]	2.17	1.54	1.18
WP Copper fraction [1]	0.783	0.808	0.832
Peak Divertor Load [MW/m^2]	4.23	3.36	3.12
Blanket Lifetime [y]	3.90	4.40	3.37
Av. neutron Wall load [MW/m2]	1.71	1.52	1.98
Capital Costs [PCU]	6340	6900	6950

Table 2: A selection of PROCESS' output parameters for the converged design point for each of the three HELIAS configurations. The design points were optimized with respect to cost of electricity and for a net electricity output of 1 GW.

4.3. PROCESS for stellarators with different coil sets

Stellarator coil optimization is, at least traditionally, carried out for a fixed magnetic configuration. For every configuration, however, there exists an infinite number of coil-sets producing (approximately) the same magnetic field [55] and choosing the right coil set is a trade-off between field accuracy and engineering constraints, such as the minimal curvature, port sizes, coil-coil distance, coil-plasma distance, engineering tolerances [56], or costs. In this section we demonstrate that stellarator-PROCESS can help judging the reactor relevance of the coil-set by providing further details, as its material usage and forces, by including coil quench constraints and by considering other plant constraints at the same time. For this purpose, we generate three exemplary coil-sets targeting a W7-X like equilibrium, using the coil optimization code FOCUS [6]. The chosen coil-sets have 30, 50, and 60 coils respectively, and their corresponding Poincaré plots are shown in Figure 11. Albeit similar flux surfaces and island positions compared to the W7-X equilibrium, further physics properties of the respective equilibriums were not checked here, as our purpose here is just an exemplary application of Process to different stellarator coil sets for the same equilibrium.

Process can now be used to scale the overall size of the machine to a reactor size machine (1 GW net electricity), while assuming that the coil-sets generate a feasible W7-X-like plasma state. Relevant coil related Process output parameters are shown in Table 3.

Using these these exemplary results, one can gain insights for the coil optimization: Using the quench restrictions and the critical current density parametrization, Process allows to calculate a coil thickness which depends on the number of coils and the distance of the coil-set from the plasma. This information can be used to specify the imposed coil-coil distance in the coil optimization step. Further, from Table 3 it also becomes clear, that the major radius for all machines is limited by the required blanket space. As in the previous section, it becomes clear from these results that coils further away from the plasma would probably be beneficial for more feasible reactor designs.

By this we demonstrate a potential use case of Process to stellarator-coil optimization, as the result allows a judgement of stellarator coils with respect to engineering quantities.

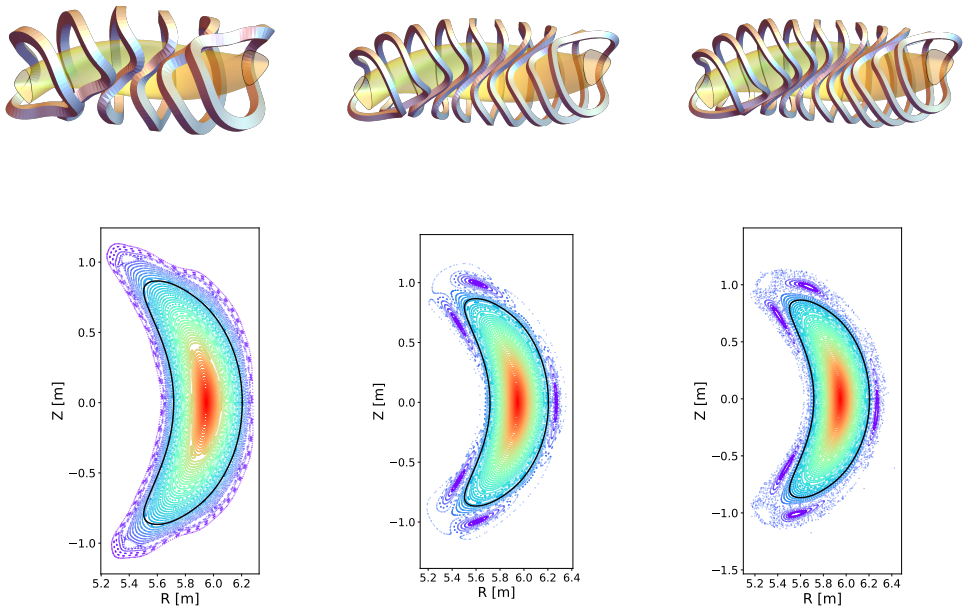

(a) (b) (c)

Figure 11: The three used scaled W7-X coil sets and their respective Poincaré plots in the bean-shaped plane as obtained with FOCUS: Left: W7-X with 30 coils (one module), Middle: W7-X with 50 coils (one module), Right: W7-X with 60 coils (one module). Coil thicknesses are scaled according to similar magnetic field on the coils ($\sim 13T$). The colour in the Poincaré plots indicates a flux surface coordinate.

Description	W7X-30	W7X-50	W7X-60
Number of tor. Field Coils [1]	30.0	50.0	60.0
Fusion Power [MW]	2990	3210	3390
Major Plasma Radius [m]	22.6	21.6	24.8
Minor Plasma Radius [m]	1.55	1.66	2.35
Aspect Ratio [1]	14.6	13.0	10.5
Plasma Volume [m^3]	1070	1170	2720
Tor. B-field [T]	5.89	5.56	4.57
Max. Field on the coils [T]	14.2	14.1	14.2
WP Current Density [MA/m^2]	2.40×10^7	3.89×10^7	4.06×10^7
j_{op}/j_{crit} [1]	0.800	0.800	0.800
Tot. Coil Mass [kg]	9.01×10^6	4.84×10^6	5.22×10^6
Max. Force Density [MN/m]	134	85.7	71.6
WP toroidal thickness [m]	0.900	0.520	0.452
WP radial thickness [m]	1.08	0.624	0.542
Coil-Coil Gap [m]	0.318	0	0
Available left radial Gap [m]	0	0	0
Max. Vertical Port Size [m]	1.93	1.13	1.09
Capital Costs [PCU]	8150	7870	9420

Table 3: The surface averaged relative field accuracy of the used coil sets and a selection of PROCESS' output parameters for the converged power plant design point of an upscaled W7-X equilibrium with 30, 50 and 60 coils respectively. The design points were optimized with respect to capital costs and for a net electricity output of 1 GW.

5. Discussion

In this paper we have presented modifications of the systems code PROCESS to model a general class of stellarators, only based on their coil-set and their respective plasma MHD equilibrium. We introduced a seperate "pre-processing" step in the workflow between stellarator optimization and usage of the actual systems code, which involves more time consuming calculations and which produces a set of configuration dependent effective parameters that we denoted as $a_i(\mathfrak{C})$, where '$\mathfrak{C}$' represents a unique stellarator configuration with coils and its reference plasma equilibrium. This pre-processing step was automatized in a separate python tool and, with the respective descriptions in the text, can be used on the coil filaments and the VMEC equilibrium as input files. We further adjusted models in PROCESS itself, to consist of exact and empirical scaling laws, based on the calculated effective parameters. In PROCESS we focussed our modifications on the transport module, the coil module, the blanket and the divertor module, the structure mass module, the build-consistency and the force module. For the modifications of these models we covered several stellarator specific features for a fusion power plant, such as the transport confinement time scaling, the island divertor configuration, the relevant density limits, the 3D coil forces, the magnetic field on the coils, the neutron inhomogeneity on the first wall, the coil curvature or the port sizes. Other stellarator specifics such as an accurate description of the alpha particle wall load in stellarators, the inhomogeneous plasma radiation load on wall materials and a 3D stress model are left out for future publications.

Given the pre-processing step, these modifications then allow for a reasonable, general treatment of stellarators in PROCESS. We demonstrated this in section 4, where we applied PROCESS in three use-cases: First, we benchmarked the results of the newly implemented coil model against the (independent) tokamak description of PROCESS. We not only found a similar optimized design point but also sufficient agreement in the relevant parameters themselves. Secondly, we applied PROCESS to three previously found configurations [52], and obtained an example optimization point with more detailed physics and engineering parameters. Further, with Nb_3Sn superconductors, the design points were found at significantly higher magnetic field, compared to the original NbTi design points, while also at smaller minor radius and lower plasma volume. In the third application, we demonstrated that the technological constraints implemented in PROCESS can be used to

provide insights in important input parameters for stellarator coil optimization, such as the coil-coil distances or the coil-plasma distance in the coil-set, which are subject to non-trivial material constraints, as superconductor properties or coil quench considerations.

The PROCESS code is maintained at the Culham Centre for Fusion Energy (CCFE) in Culham, Oxfordshire, UK (A description of the code can be found here: `https://ccfe.ukaea.uk/resources/process/`). The "pre-processing" step was implemented as a python tool, which is maintained at the Max-Planck-Institute for Plasmaphysics in Greifswald, Germany.

Acknowledgement

This work has been carried out within the framework of the EUROfusion Consortium and has received funding from the Euratom research and training programme 2014–2018 and 2019–2020 under grant agreement No 633053, and from the RCUK under grant number EP/T012250/1. The views and opinions expressed herein do not necessarily reflect those of the European Commission. The author would like to thank the PROCESS-team for their support with the code, Joachim Geiger for equilibrium calculations of the HELIAS configurations, Jiawu Zhu and Victor Bykov for support with engineering questions and Caoxiang Zhu for access and support with FOCUS.

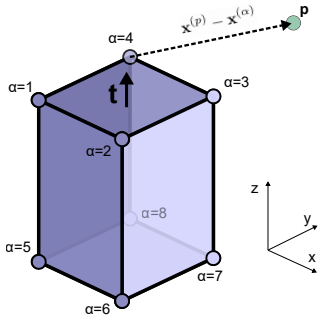

Figure A.12: Nomenclature of the formulas in the text: A straight cuboid, carrying a homogenous current (Beam) is parametrized by 8 points. Those points are indexed by α in the text. The current flows in $\mathbf{t}$ direction. The $\mathbf{B}$ field at the point $\mathbf{p}$ is derived in the text.

Appendix A. Biot-Savart with finite conductor size

Here we derive the magnetic field B at a point $\mathbf{p}$ due to a current carrying rectangular cuboid (Beam) as shown schematically in Figure A.12. This method was also used in [44] e.g. When a 3D stellarator is approximated by N such Beams this procedure allows a fast evaluation of the magnetic field near and in the conductor.

$\mathbf{b}$ is the vector in longitudinal (y-) direction of the Beam, while $\mathbf{n}$ points in normal (x-) direction. Define the functions:

$$F_1(\mathbf{p}) = \int_{-h}^{h} dy \int_{-b}^{b} dx \frac{y_p - y}{N(x - x_p, y - y_p, z)^3} \tag{A.1}$$

$$F_2(\mathbf{p}) = \int_{-h}^{h} dy \int_{-b}^{b} dx \frac{x_p - x}{N(x - x_p, y - y_p, z)^3} \tag{A.2}$$

$$N(x, y, z) = \sqrt{z^2 + y^2 + x^2} \tag{A.3}$$

where x_p are projections according to: $x_p = \mathbf{p} \cdot \mathbf{e}_x$. $2b$ is the dimension of the Beam in x and $2d$ in y direction.

If the current density in the winding pack is approximated as a continuous constant function across a rectangular cross section, pointing w.l.o.g. in Cartesian z direction, Biot-Savart's volume integral can be written as:

$$\mathbf{B}^{\text{Beam}}(\mathbf{p}) = \frac{\mu_0 |\mathbf{j}_0|}{4\pi} \int dz \left[F_1(\mathbf{p}) \mathbf{e}_x - F_2(\mathbf{p}) \mathbf{e}_y \right]. \tag{A.4}$$

The integral over F_1 and F_2 have an analytical form then, as it is shown below.

For convenience, define

$$F(x, A, B) \equiv \int \frac{dx}{\sqrt{x^2 + A^2 + B^2}} = \operatorname{arctanh}\left(\frac{x}{\sqrt{A^2 + B^2 + x^2}}\right), \tag{A.5}$$

and (note the changed order of the arguments)

$$\begin{aligned} I(A, B, x) &\equiv \int dx F(A, B, x) \\ &= x\, F(A, B, x) - x + AF(x, B, A) \\ &- |B| \arctan\left(\frac{B^2 + A(A + \sqrt{x^2 + A^2 + B^2})}{|B|x}\right). \end{aligned} \tag{A.6}$$

Then

$$\begin{aligned} F_1(\mathbf{p}) &= \int_{-d}^{d} dy \int_{-b}^{b} dx\, \partial_y \left[\frac{1}{\sqrt{(x - x_p)^2 + (y - y_p)^2 + z^2}}\right] \\ &= \int_{-b}^{b} dx \left[\frac{1}{N(x - x_p, d - y_p, z)} - \frac{1}{N(x - x_p, -d - y_p, z)}\right] \\ &= F(b - x_p, d - y_p, z) - F(-b - x_p, d - y_p, z) \\ &- F(b - x_p, -d - y_p, z) + F(-b - x_p, -d - y_p, z). \end{aligned} \tag{A.7}$$

And analogously for F_2 it is

$$\begin{aligned} F_2(\mathbf{p}) &= F(d - y_p, b - x_p, z) - F(-d - y_p, b - x_p, z) \\ &- F(d - y_p, -b - x_p, z) + F(-d - y_p, -b - x_p, z). \end{aligned} \tag{A.8}$$

This simplifies Equation A.4 to a one dimensional integral along the z-direction, which can be solved numerically. However, using Equation A.6, the integral in z-direction can also be solved analytically, and the magnetic

field $\mathbf{B}$ can then be written as

$$\begin{aligned}\mathbf{B}^{\text{Beam}}(\mathbf{p}) = \frac{\mu_0|\mathbf{j}_0|}{4\pi}\Bigg[\mathbf{e}_x\Big[&I(b-x_p,d-y_p,h) - I(-b-x_p,d-y_p,h)\\ &- I(-b-x_p,-d-y_p,h) + I(-b-x_p,-d-y_p,h)\\ &- I(b-x_p,d-y_p,-h) - I(-b-x_p,d-y_p,-h)\\ &- I(-b-x_p,-d-y_p,-h) + I(-b-x_p,-d-y_p,-h)\Big]\\ &- \mathbf{e}_y\Big[I(d-y_p,b-x_p,h) - I(d-y_p,-b-x_p,h)\\ &- I(-d-y_p,-b-x_p,h) + I(-d-y_p,-b-x_p,h)\\ &- I(d-y_p,b-x_p,-h) - I(d-y_p,-b-x_p,-h)\\ &- I(-d-y_p,-b-x_p,-h) + I(-d-y_p,-b-x_p,-h)\Big]\Bigg].\end{aligned} \tag{A.9}$$

The magnetic field at a point $\mathbf{p}$ due to a coil with finite size can be obtained by a simple Riemann sum over the contribution of every Beam $\mathbf{B}_i^{\text{Beam}}$:

$$\mathbf{B}_{\text{coil}}(\mathbf{p}) = \int_{\text{coil}} d\mathbf{B}(\mathbf{p}) \simeq \sum_i \mathbf{B}_i^{\text{Beam}}(\mathbf{p}) \tag{A.10}$$

The accuracy of Equation A.10 depends on the number of discretization points, see Figure A.13 and lies in the order of $\Delta B/B \sim 10^{-4}$.

Appendix B. Quench Protection

We shortly provide the derivation of the critical current density as limited by a simple coil quench protection argument as given in the final form in [20].

In thermal equilibrium and without losses the heat produced by the copper resistivity during a quench is equal to the heat needed to rise the temperature in the material by dT:

$$dQ_{heat} = dQ_{temp} \tag{B.1}$$

Assuming the materials in the winding pack are thermally equilibrated Equation B.1 is

$$P(t)dt = \sum_i c_i \rho_i V_i \, dT, \tag{B.2}$$

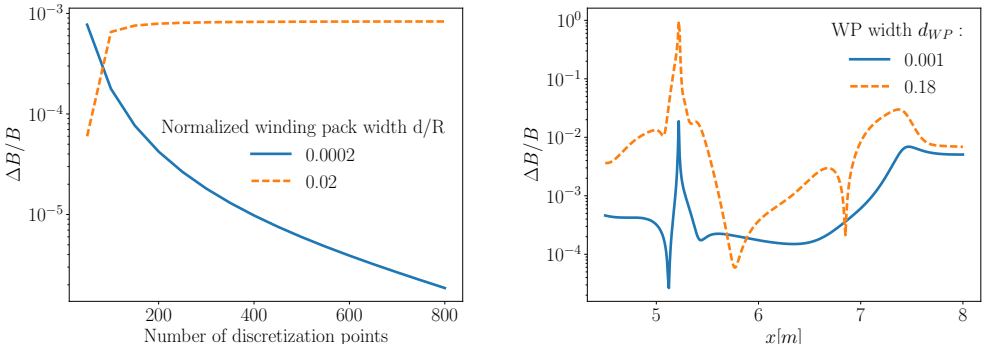

Figure A.13: Left: The relative field error of Equation A.10 compared to the analytical correct $\mu_0 I/(2\pi R)$, plotted against different number of discretization points in the centre of an ideal toroid. Right: Comparison of magnetic field strength values from Equation A.10 in the bean shaped plane of W7-X at $z = 0$ against values calculated by an independent *filament* Biot-Savart integration. The dashed line in both plots show deviations by a significant coil thickness.

where P is the power produced by the copper current in time t, i runs over all winding pack materials and V_i stands for the volume of the ith material. With $P = J^2 \eta V$, where η is the resistivity, Equation B.2 becomes

$$J(t)^2 dt = \sum_i \frac{c_i \rho_i}{\eta_{Cu}(T)} \frac{V_i}{V_{Cu}} \, dT, \tag{B.3}$$

Now, the quench restriction is to *impose*

$$\int J(t)^2 dt \overset{!}{<} \int_{T_{op}}^{T_{max}} \sum_i \frac{c_i \rho_i}{\eta_{Cu}(T)} f_i \, dT. \tag{B.4}$$

The integral on the left hand side runs over the whole quench time while the integral on the right hand side goes from the operation temperature T_{op} to a maximal T_{max}. The difference $T_{max} - T_{op}$ is usually chosen in the order of 150 K.

If one assumes an exponential decay of J after a quench detection time t_d as:

$$J(t) = \begin{cases} J_0, & \text{if } t < t_d \\ J_0 \, e^{-\frac{t - t_d}{\tau_{dump}}}, & \text{otherwise} \end{cases} \tag{B.5}$$

then, $\int J(t)^2 dt = J_0^2 \left(\frac{1}{2}\tau_{dump} + t_d\right)$ (J_0 is the initial current density), one gets

$$\frac{1}{2} J_0^2 \tau_{dump} < q_{Cu} + \frac{V_{He}}{V_{Cu}} q_{He} + \frac{V_{scu}}{V_{Cu}} q_{scu}, \tag{B.6}$$

with

$$q_{Cu} \equiv \int_{T_0}^{T_{max}} \frac{\rho_{Cu} c_{Cu}}{\eta_{Cu}(T)}\, dT \tag{B.7}$$

$$q_{He} \equiv \int_{T_0}^{T_{max}} \frac{\rho_{He}(T) c_{He}(T)}{\eta_{Cu}(T)}\, dT \tag{B.8}$$

$$q_{scu} \equiv \int_{T_0}^{T_{max}} \frac{\rho_{scu} c_{scu}}{\eta_{Cu}(T)}\, dT. \tag{B.9}$$

Using the definition of the relative winding pack material fractions f as in Equation 48 the volume fractions can be rewritten in terms of the conduit volume V_{conduit}:

$$V_{Cu} = V_{\text{conduit}} \left(1 - f_{He}\right) f_{Cu} \tag{B.10}$$

$$V_{He} = V_{\text{conduit}}\, f_{He} \tag{B.11}$$

$$V_{scu} = V_{\text{conduit}} \left(1 - f_{He}\right) \left(1 - f_{Cu}\right). \tag{B.12}$$

With this, one ends up with (identifying J_0 with the copper current J_{cu})

$$J_{cu} < \sqrt{\frac{1}{\left(\frac{1}{2}\tau_{dump} + t_d\right)} \left(q_{cu} + \frac{f_{He}}{(1 - f_{He}) f_{Cu}} q_{He} + \frac{1 - f_{Cu}}{f_{Cu}} q_{scu}\right)}. \tag{B.13}$$

In terms of the total winding pack current density, Equation B.13 can be rewritten using $1 - f_{He} = f_{cond}$ and $J_{WP} = J_{Cu} f_{Cu} f_{cond} (1 - f_{case})$:

$$J_{WP} < (1 - f_{case}) \sqrt{\frac{1}{\left(\frac{1}{2}\tau_{dump} + t_d\right) \eta} \left(f_{Cu}^2 f_{cond}^2 q_{cu} + f_{Cu} f_{cond} (1 - f_{cond}) q_{He} + f_{Cu} f_{cond}^2 (1 - f_{Cu}) q_{scu}\right)} \tag{B.14}$$

Equation B.14 constraints the winding pack current density by a temperature rise during a coil quench. This value is dependent on the chosen copper alloy, which enters in η and c_i.

References

[1] Pedersen, T.S. et al, Confirmation of the topology of the wendelstein 7-x magnetic field to better than 1:100,000, Nature Communications 7 (1). doi:10.1038/ncomms13493.

[2] Lazerson, S.A., Otte, M., Bozhenkov, S., Biedermann, C. and PedersenIS, T.S., First measurements of error fields on w7-x using flux surface mapping, Nuclear Fusion 56 (10) (2016) 106005. doi:10.1088/0029-5515/56/10/106005.

[3] Drevlak, M., Beidler, C., Geiger, J., Helander, P. and Turkin, Y., Optimisation of stellarator equilibria with ROSE, Nuclear Fusion 59 (1) (2018) 016010. doi:10.1088/1741-4326/aaed50.

[4] Gates, D. et al, Recent advances in stellarator optimization, Nuclear Fusion 57 (12) (2017) 126064. doi:10.1088/1741-4326/aa8ba0.

[5] Landreman, M., Sengupta, W. and Plunk, G.G., Direct construction of optimized stellarator shapes. part 2. numerical quasisymmetric solutions, Journal of Plasma Physics 85 (1). doi:10.1017/s0022377818001344.

[6] Zhu, C., Hudson, S.R., Song, Y. and Wan, Y., Designing stellarator coils by a modified newton method using FOCUS, Plasma Physics and Controlled Fusion 60 (6) (2018) 065008. doi:10.1088/1361-6587/aab8c2. URL https://doi.org/10.1088%2F1361-6587%2Faab8c2

[7] Lazerson, S., Schmitt, J., Zhu, C., Breslau, J. and STELLOPT Developers, A., Stellopt (2020). doi:10.11578/DC.20180627.6.

[8] Kovari, M., Kemp, R., Lux, H., Knight, P., Morris, J. and Ward, D., Process: A systems code for fusion power plants - part 1: Physics, Fusion Engineering and Design 89 (2014) 3054.

[9] Reux, C. et al, DEMO reactor design using the new modular system code SYCOMORE, Nuclear Fusion 55 (7) (2015) 073011. doi:10.1088/0029-5515/55/7/073011.

[10] Franza, F., Development and validation of a computational tool for fusion reactors' system analysisdoi:10.5445/IR/1000095873.

[11] Coleman, M. and McIntosh, S., BLUEPRINT: A novel approach to fusion reactor design, Fusion Engineering and Design 139 (2019) 26–38. doi:10.1016/j.fusengdes.2018.12.036.

[12] Federici, G., Biel, W., Gilbert, M., Kemp, R., Taylor, N. and Wenninger, R., European DEMO design strategy and consequences for materials, Nuclear Fusion 57 (9) (2017) 092002. doi:10.1088/1741-4326/57/9/092002.

[13] Federici, G. et al, DEMO design activity in europe: Progress and updates, Fusion Engineering and Design 136 (2018) 729–741. doi:10.1016/j.fusengdes.2018.04.001.

[14] Wenninger, R. et al, The physics and technology basis entering european system code studies for demo, Nuclear Fusion 57 (1) (2016) 016011.

[15] Warmer, F. et al, Helias module development for systems codes, Fusion Engineering and Design 91 (2014) 60. doi:http://doi.org/10.1016/j.fusengdes.2014.12.028.

[16] Warmer, F. et al, Implementation and verification of a helias module for the systems code process, Fusion Engineering and Design 98-99 (2014) 2227. doi:http://doi.org/10.1016/j.fusengdes.2014.12.021.

[17] Warmer, F. et al, Systems code analysis of helias-type fusion reactor and economic comparison to tokamaks, IEEE Transactions on Plasma Science 44 (2016) 1576–1585.

[18] Schauer, F., Egorov, K. and Bykov, V., Helias 5-b magnet system structure and maintenance concept, Fusion Engineering and Design 88 (2013) 1619.

[19] Yamada, H. et al, Characterization of energy confinement in net-current free plasmas using the extended international stellarator database, Nuclear Fusion 45 (2005) 1684.

[20] Kovari, M., Fox, F., Harrington, C., Kembleton, R., Knight, P., Lux, H. and Morris, J., "process": A systems code for fusion power plants – part 2: Engineering, Fusion Engineering and Design 104 (2016) 9–20. doi:https://doi.org/10.1016/j.fusengdes.2016.01.007.

[21] Lux, H., Kemp, R., Ward, D. and Sertoli, M., Impurity radiation in DEMO systems modelling, Fusion Engineering and Design 101 (2015) 42–51. doi:10.1016/j.fusengdes.2015.10.002.

[22] Lux, H., Kemp, R., Fable, E. and Wenninger, R., Radiation and confinement in 0d fusion systems codes, Plasma Physics and Controlled Fusion 58 (7) (2016) 075001. doi:10.1088/0741-3335/58/7/075001.

[23] Calvo, I., Parra, F.I., Velasco, J.L. and Alonso, J.A., Stellarators close to quasisymmetry, Plasma Physics and Controlled Fusion 55 (12) (2013) 125014.
URL http://stacks.iop.org/0741-3335/55/i=12/a=125014

[24] Beidler, C.D. et al, Benchmarking of the mono-energetic transport coefficients - results from the international collaboration on neoclassical transport in stellarators (icnts), Nuclear Fusion 51 (2011) 076001. doi:http://doi.org/10.1088/0029-5515/51/7/076001.

[25] Sudo, S., Takeiri, Y., Zushi, H., Sano, F., Itoh, K., Kondo, K. and Iiyoshi, A., Scalings of energy confinement and density limit in stellarator/heliotron devices, Nuclear Fusion 30 (1) (1990) 11.
URL http://stacks.iop.org/0029-5515/30/i=1/a=002

[26] Miyazawa, J. et al, Density limit study focusing on the edge plasma parameters in lhd, Nuclear Fusion 48 (1) (2008) 015003.
URL http://stacks.iop.org/0029-5515/48/i=1/a=015003

[27] Fuchert, G. et al, Increasing the density in wendelstein 7-x: benefits and limitations, Nuclear Fusion 60 (3) (2020) 036020. doi:10.1088/1741-4326/ab6d40.

[28] Preinhaelter, J., Penetration of an ordinary wave into a weakly inhomogeneous magnetoplasma at oblique incidence, Czechoslovak Journal of Physics 25 (1) (1975) 39–50. doi:10.1007/bf01589670.

[29] Hansen, F.R., Lynov, J.P. and Michelsen, P., The o-x-b mode conversion scheme for ECRH of a high-density tokamak plasma, Plasma Physics and Controlled Fusion 27 (10) (1985) 1077–1100. doi:10.1088/0741-3335/27/10/002.

[30] Ohyabo, N. et al, The large helical device (lhd) helical divertor, Nuclear Fusion 34 (1994) 387.

[31] Bader, A., Boozer, A.H., Hegna, C.C., Lazerson, S.A. and Schmitt, J.C., HSX as an example of a resilient non-resonant divertor, Physics of Plasmas 24 (3) (2017) 032506. doi:10.1063/1.4978494.

[32] Grigull, P. et al, First island divertor experiments on the w7-AS stellarator, Plasma Physics and Controlled Fusion 43 (12A) (2001) A175–A193. doi:10.1088/0741-3335/43/12a/313.

[33] Koenig, R. et al, The divertor program in stellarators, Plasma Physics and Controlled Fusion 44 (11) (2002) 2365–2422. doi:10.1088/0741-3335/44/11/306.

[34] Pedersen, T.S. et al, First results from divertor operation in wendelstein 7-x, Plasma Physics and Controlled Fusion 61 (1) (2018) 014035. doi:10.1088/1361-6587/aaec25.
URL https://doi.org/10.1088%2F1361-6587%2Faaec25

[35] Feng, Y. et al, On the w7-x divertor performance under detached conditions, Nuclear Fusion 56 (12) (2016) 126011. doi:10.1088/0029-5515/56/12/126011.

[36] Feng, Y., Kobayashi, M., Lunt, T. and Reiter, D., Comparison between stellarator and tokamak divertor transport, Plasma Physics and Controlled Fusion 53 (2011) 024009.

[37] Stangeby, P., The Plasma Boundary of Magnetic Fusion Devices, CRC Press, 2000. doi:10.1201/9780367801489.

[38] Feng, Y., Up-scaling the island divertor along the w7-stellarator line, Journal of Nuclear Materials 438 (2013) S497.

[39] Rosenbluth, M., Sagdeev, R., Taylor, J. and Zaslavski, G., Destruction of magnetic surfaces by magnetic field irregularities, Nuclear Fusion 6 (4) (1966) 297–300. doi:10.1088/0029-5515/6/4/008.

[40] A Li Puma, F. Franza, L.V.B., Wp12-sys01-t02 - model improvements (blanket model), EUROfusion, IDM (EFDA_D_2LKMCT).

[41] Bosch, H.S. and Hale, G.M., Improved formulas for fusion cross-sections and thermal reactivities, Nuclear Fusion 32 (1992) 611.

[42] Häußler, A., Fischer, U. and Warmer, F., Verification of different monte carlo approaches for the neutronic analysis of a stellarator, Fusion Engineering and Design 124 (2017) 1207–1210. doi:10.1016/j.fusengdes.2017.04.010.

[43] Bozhenkov, S., Geiger, J., Grahl, M., Kißlinger, J., Werner, A. and Wolf, R., Service oriented architecture for scientific analysis at w7-x. an example of a field line tracer, Fusion Engineering and Design 88 (11) (2013) 2997–3006. doi:10.1016/j.fusengdes.2013.07.003.

[44] Sackett, S.J., Effi: A code for calculating the electromagnetic field, force, and inductance in coil systems of arbitrary geometry, Unknown.

[45] Urankar, L., Vector potential and magnetic field of current-carrying finite arc segment in analytical form, part III: Exact computation for rectangular cross section, IEEE Transactions on Magnetics 18 (6) (1982) 1860–1867. doi:10.1109/tmag.1982.1062166.

[46] Schauer, F., Coil winding pack fe-analysis for a helias reactor, Fusion Engineering and Design 86 (2011) 636.

[47] Neumann, F.E., Allgemeine gesetze der inducirten elektrischen ströme, Annalen der Physik und Chemie 143 (1) (1846) 31–44. doi:10.1002/andp.18461430103.

[48] Dengler, R., Self inductance of a wire loop as a curve integral, Advanced Electromagnetics 5 (1) (2016) 1. doi:10.7716/aem.v5i1.331.

[49] Cumyn, P.B. and Rosen, J.P.F., Engineering features of the tokamak de varennes, in: Fusion technology 1988. V. 1, 1989.

[50] Jaksic, N., Mendelevitch, B. and Tretter, J., Alternative conceptual design of a magnet support structure for plasma fusion devices of stellarator type, Fusion Engineering and Design 86 (6-8) (2011) 689–693. doi:10.1016/j.fusengdes.2011.01.139.

[51] Moon, F.C., The virial theorem and scaling laws for superconducting magnet systems, Journal of Applied Physics 53 (1982) 9112.

[52] Andreeva, T. et al, The helias reactor concept: Comparative analysis of different field period configurations, Fusion Science and Technology 46 (2) (2004) 395–400. doi:10.13182/fst04-a579.

[53] Bader, A. et al, Stellarator equilibria with reactor relevant energetic particle losses, Journal of Plasma Physics 85 (5). doi:10.1017/s0022377819000680.

[54] Henneberg, S., Drevlak, M., Nührenberg, C., Beidler, C., Turkin, Y., Loizu, J. and Helander, P., Properties of a new quasi-axisymmetric configuration, Nuclear Fusion 59 (2) (2019) 026014. doi:10.1088/1741-4326/aaf604.
URL https://doi.org/10.1088%2F1741-4326%2Faaf604

[55] Landreman, M., An improved current potential method for fast computation of stellarator coil shapes, Nuclear Fusion 57 (4) (2017) 046003. doi:10.1088/1741-4326/aa57d4.

[56] Lobsien, J.F., Drevlak, M. and and, T.S.P., Stellarator coil optimization towards higher engineering tolerances, Nuclear Fusion 58 (10) (2018) 106013. doi:10.1088/1741-4326/aad431.
URL https://doi.org/10.1088%2F1741-4326%2Faad431